Letter

Athermal sediment creep triggered by porous flow

M. Houssais*
Levich Institute, City College of CUNY, 140th Street and Convent Avenue, New York, New York 10031, USA

Charles Maldarelli and Jeffrey F. Morris
Levich Institute and Chemical Engineering Department, City College of CUNY, 140th Street and Convent Avenue, New York, New York 10031, USA

(Received 8 March 2020; revised 21 September 2020; accepted 8 December 2020; published 4 January 2021)

The dynamics of sediment creep under the stress of a porous flow, a situation ubiquitous in the environment, remains scarcely studied. To initiate such effort, experiments of a submerged quasi-two-dimensional sediment layer creeping downslope were performed, varying the setup tilt and a porous flow under the two respective thresholds for yielding. Logarithmic decay rates of the deformation are observed, with the rate increasing with both control parameters. A new dimensionless parameter, P^*, accounting for the mean porous flow intensity and the distance to the yield stress, is proposed and allows a collapse of all the deformation results on a single curve. Two distinct creep regimes are identified and correspond to a weak but systematic change of the mean void size as P^* increases.

DOI: 10.1103/PhysRevFluids.6.L012301

Disordered particulate media such as granular materials, foams, or glasses, are subject to creep—small particle rearrangements happening over long timescales. These localized deformations take place at conditions under the known yield criterion and accumulate over time, resulting in aging of concrete [1], bending of metallic girders [2], and the rounding of sedimentary landscapes [3–5].

Static heaps of frictional athermal particles classically exhibit a surface angle defining the yield criterion. Under that critical angle, avalanching flows do not occur anymore, and all heap of a certain granular material exhibit the same geometry. Yet, near their yield criterion, as for many other amorphous materials, a hysteretic behavior is observed, and two characteristic angles can be measured, for onset (θ_{start}) and cessation ($\theta_{\text{stop}} < \theta_{\text{start}}$) of avalanches. Criterion values generally depend on the system's size [6]; and, under small perturbations, the system may relax (or creep) at stresses far below the criterion, via localized plastic events [7–11].

Athermal granular creep rate was recently shown to be sustained over time by small mechanical stress oscillations [8], while the yield criterion can be overcome by the presence of vibrations [9], or the proximity of shear zones [12,13]. These phenomenologies relate to key concepts of continuous models centered on nonlocal effects, namely, the existence of localized deformation, or soft spots, and of a correlation length scale diverging near the yield stress [14–18]. Yet, our understanding at the microscopic scale remains far from complete, and more specifically, how distribution of small local forces affect the creep rate is still unclear.

Recently, Bérut *et al.* [11], explored heap granular creep in the limit where the thermal agitation force is still small compared to gravity (i.e., for Péclet number $\text{Pe} > 1$, allowing particles to sediment) but sufficient to trigger creep. Interestingly, the observed trends of creep deformation could be explained simply scaling as Pe^{-1}.

*houssais.morgane@gmail.com

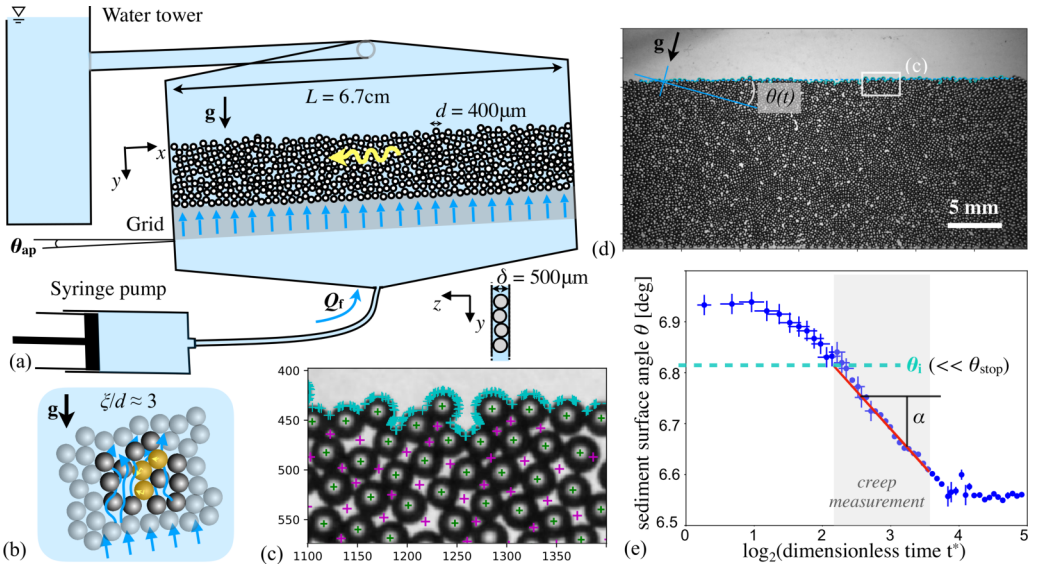

FIG. 1. (a) Sketches of the experiment (top) from the camera point of view and (bottom) from the side. (b) Sketch of local fluid flow triggering a particle rearrangement of size $\xi \simeq 3d$. (c) Example of image analysis results. Cyan crosses mark the detected bed surface elevation; green and magenta crosses are the detected particle centers and void centers, respectively. (d) Example of an analyzed image region and its whole detected bed surface. (e) Result of bed surface angle decay over time due to downslope creep, for an experiment performed at $\theta_{ap} = 6^\circ$ and $P_{drag}/P_0 = 0.045$.

In this Letter, we initiate the investigation on how porous flows, a pervasive phenomenon in natural sediments, can affect the granular creep behavior. Specifically we study how quasi-two-dimensional (quasi-2D) heaps made of athermal hard spherical particles deform under the yield criterion as they are traversed by a controlled porous flow, as sketched Figs. 1(a) and 1(b). Studying such dynamics is of fundamental interest because porous flows, unlike shear zones, stress the system via the network of voids between grains, but, unlike thermal agitations or vibrations, keep and strongly depend on the contact network geometry. We experimentally probe the athermal granular creep dynamics under porous flow conditions, thereby enhancing the understanding of subyield particulate system deformation.

Previous work in the same setting studied the dynamics of a horizontal sediment layer subjected to an upward porous flow at a range of intensities crossing the threshold over which a cavity systematically grows into a vertical channel [10]. Particles exhibited rearrangements for porous flows under the channelization criterion, showing the emergence of a net particle lateral position fluctuation, and compaction (also recently observed in a three-dimensional system [19]). These studies show that porous flow has a very nonlinear effect on granular systems, causing compaction via small rearrangement at small flow rates, until, abruptly, causing dilation which evolves into a local erosion instability at flow rates above the channelization criterion.

In the work presented here, the effect of slope is central, as we explore sediment downslope creep under the combined influence of weak porous flow and the apparatus tilt $\theta_{ap} < \theta_{stop}$. The setup angle induces a sediment surface angle $\theta > 0$, which sets the main shear stress $\sigma \propto \sin\theta$, from gravity acting on the particles. For this particular setup, we determined $\theta_{stop} = 32 \pm 0.5^\circ$ (see details in Appendix A and Supplemental Material Fig. 1 [20]).

The apparatus is a PDMS microfluidic cell of dimensions $L \times H \times \delta = 67$ mm $\times$ 25 mm $\times$ 0.5 mm, filled entirely with water (viscosity $\eta = 0.001$ Pa s) and a quasi-2D layer of polystyrene particles of mean diameter $d = 0.4$ mm [see Fig. 1(a)] and projected area $S_p = \pi(d/2)^2$. The mean

stress resulting from an individual particle weight is defined as $P_0 = F_{\text{gravity}}/2Sp = \Delta\rho g d/3$, with the gravitational acceleration, g, and the density difference $\Delta\rho = \rho_{\text{particle}} - \rho_{\text{water}} = 50\,\text{kg}\,\text{m}^{-3}$ [21]. The layer of particles rests on a grid made up of 0.5-mm-diameter pylons separated by 0.3 mm, and the side walls of the channel are roughened, using a pattern mimicking the grid surface roughness. The surfaces of the front and back walls are made hydrophilic by silanization. The quasi-2D configuration allows for all voids to be visible [see Fig. 1(c)]. The sediment bed height is always about $40d$, and its width is $168d$. To avoid significant lateral wall effects in the long dimension [x direction in Fig. 1(a)], particle dynamics were observed at the center of the image, over a region of $50d \times 100d$, as shown in Fig. 1(d).

For each realization the same protocol was followed. First the sediment layer was prepared flat and horizontal by a fixed series of successive tilts and resuspensions, then the apparatus was tapped once on the side, and the system was kept at rest and aged for 5 min. Then the camera (EOS Rebel T3i) and syringe pump (Harvard PHD2000) were simultaneously started, taking images and injecting a constant fluid discharge Q_f through the bed. At the same time, the apparatus tilt was set from 0 to the angle $\theta_{\text{ap}} > 0$. The hydrostatic pressure inside the system was maintained constant over all the experiments by a water tower whose water surface level was kept at a fixed distance from the center of the channel. The range of flow discharge explored is $70 < Q_f < 285$ μl/min.

Images were taken every 4 s for the first 5 min of the experiments, and then every 28 s for the following hours. Experiment durations were limited by the syringe volume (10 ml) and varied from 6 to 250 min. Image resolution is on average 855 pixels per particle projected area S_p, and allows for all voids to be detected. On each image, the bed surface, particle centers, and thereafter void sizes were detected using open access OPENCV and TRACKPY [10,22]. Typical detection results are shown in Figs. 1(c) and 1(d) (see Supplemental Material Fig. 2 for initial packing fraction measurements).

The experiment geometry is a squared box in order to study the effect of a porous flow in its simplest form. Unlike for drum experiments, it then requires one to measure the creep dynamics over a small amount of deformation, in order to maintain the porous flow condition about constant. In addition, field data have shown that soil creep fluxes were proportional to the soil surface slope [23]. For these reasons, we performed six series of experiments at different apparatus angles $\theta_{\text{ap}} = 27$, 21, 15, 9, 6, and 3° (±0.5°), all significantly lower than the critical angle found in the absence of flow $\theta_{\text{stop}} \simeq 32°$.

For each experimental series, the imposed flow discharge Q_f is varied, and each set of control parameters $(\theta_{\text{ap}}, Q_f)$ was repeated three times. A same phenomenology is systematically observed: as the fluid flows through the quasistatic granular layer—with a distribution of contact forces on particles [see Fig. 1(b)]—the resulting distribution of small drag forces causes some particles to rearrange. The individual-particle and small-group motions eventually lead to collective downslope motion. For larger slope and flow rate, the collective rearrangements are also larger and quicker. Conversely, at very low angle and flow discharge, collective rearrangements—if any occur—are less frequent and smaller, although the entire settled layer often demonstrates slow compaction, as previously observed for horizontal experiments [10,19]. See Supplemental Material videos presenting diverse cases [20].

While weak porous flows develop a distribution of oriented drag forces on the particles composing the sediment bed, weak thermal force is isotropic and constant with particle weight. Despite these significant differences, to start deciphering the nature of the porous flow capacity to trigger granular creep in the athermal regime ($\text{Pe} = mgd/k_bT \simeq 10^9$ in our experiments), we compare our observations to the slightly thermal case ($\text{Pe} \simeq 10$–100) explored by Bérut *et al.* [11].

The detected bed surface is fitted by a line to measure the bed surface angle over time $\theta(t)$, as shown in Fig. 1(d). At any time and depth Δy, the shear stress imposed is $\sigma = \Delta\rho g \Delta y \sin\theta$. Additionally the sediment bed perceives, due to drag forces acting on particles, the average dimensionless pressure in the direction opposed to gravity:

$$\frac{P_{\text{drag}}}{P_0} = \frac{9\eta U_{\text{bed}} \cos\theta_{\text{ap}}}{\Delta\rho g d^2} \propto \frac{F_{\text{drag}}}{F_{\text{gravity}}},$$

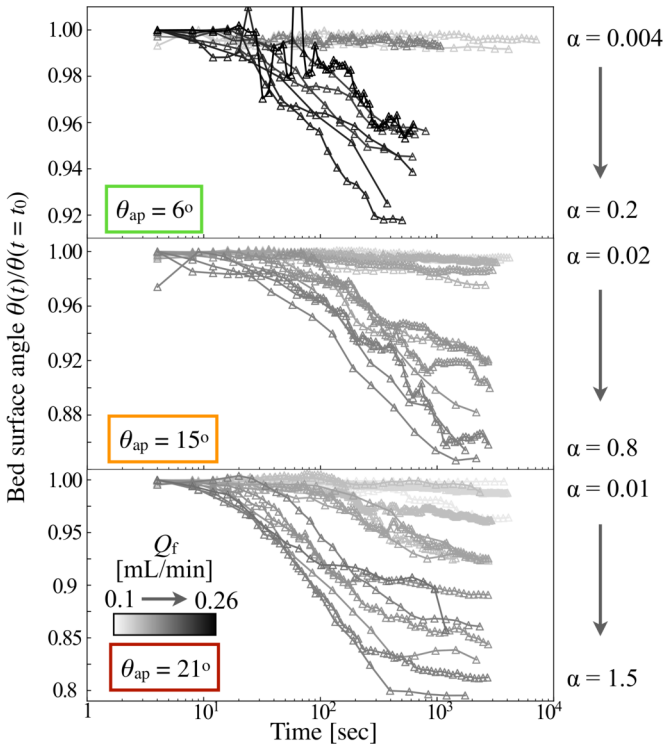

FIG. 2. Evolution of the sediment layer surface slope with time, for the series performed at $\theta_{ap} = 6°$, 15°, and 21°. Data are normalized by the slope angle value θ at $t_0 = 6$ s. The curves gray level scales with the flow discharge Q_f.

with P_0 the stress from a single particle weight, and the initial mean flow velocity inside the bed $U_{bed} = Q_f/[(1 - \langle\Phi\rangle)\delta L]$, with $\langle\Phi\rangle$ the packing fraction from image analysis averaged over the time period during which creep is measured. For all our experiments, we found that the mean value of $\langle\Phi\rangle$ is 0.68, and its standard deviation is 0.02. The subsequent normalization of time by P_{drag}/P_0 takes into account the net effect of the flow mean stress on the bed, although it remains far below the criterion to lift a particle for all our experiments ($0 \leqslant P_{drag}/P_0 < 0.06$). The range of mean flow velocity U_{bed} explored was 0.1–0.45 mm s^{-1}. Using $\Delta y = d$, one can derive the shear stress normalized by the normal stresses acting on particles at the surface: $\sigma^* = (\Delta\rho g d \sin\theta)/(\Delta\rho g d \cos\theta - P_{drag}) = \tan\theta/(1 - P_{drag}/(P_0 \times 3\cos\theta\cos\theta_{ap}))$. The dimensionless critical stress for avalanching, or yield criterion, is defined as $\sigma_c^* = \tan\theta_{stop} = 0.62 \pm 0.01$. As we explore the dynamics of the system for values of $P_{drag}/P_0 \leqslant 0.05$, σ^*/σ_c^* stays close to $\tan\theta/\tan\theta_{stop}$, and increasingly so for $\Delta y > d$.

Figure 2 shows a subset of the data of bed surface slope evolution with time, at three apparatus tilt angles, namely, $\theta_{ap} = 6$, 15, and 21°, at flow discharges for which deformation was detectable. The gray scale represents the intensity of the flow discharge Q_f. Beyond a certain flow discharge, for each θ_{ap}, a decay of bed surface angle with time could be observed. The most rapid period of decay typically exhibited a logarithmic trend $\theta \propto -\ln(t)$, with, as expected, faster decay at higher flow discharge Q_f.

Such a dependence of subcritical deformation on the logarithm of time is a known signature of creep [8,24,25]; for similar heap experiments, Bérut *et al.* [11] found decay rates inversely proportional to the Péclet number. In our case, the creep dynamics is triggered by small values of the parameter P_{drag}/P_0.

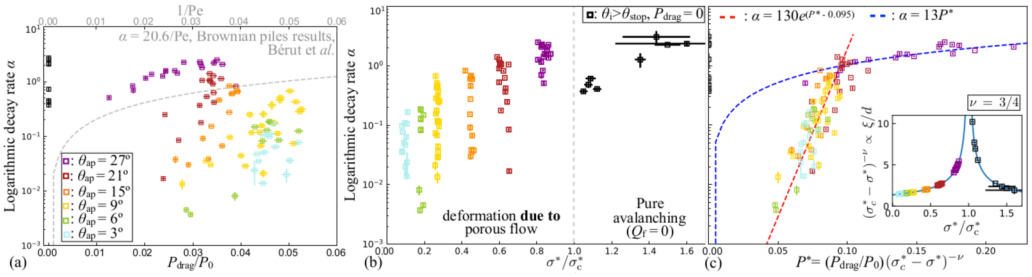

FIG. 3. Logarithmic decay of the surface slope of athermal pile ($1/\mathrm{Pe} = 10^{-9}$) with dimensionless time t^*, α, (a) as a function of the normalized mean porous flow stress on particles, P_{drag}/P_0. The dashed gray line shows results from experimental pile creep triggered by slight Brownian agitation, where α scales as Pe^{-1}. (b) α as a function of the stress ratio $\sigma^*/\sigma_c^* \simeq \tan\theta_i/\tan\theta_{\mathrm{stop}}$, and (c) as a function of the parameter P^* defined in (1), using $\nu = 3/4$. Red and blue dashed lines visually indicate an exponential and a linear trend, respectively. Inset: values of $(\sigma_c^* - \sigma^*)^{-3/4}$ reported as a function σ^*/σ_c^* in our experiments; the cyan line is the corresponding analytical form.

When the fastest decay persisted over more than an order of magnitude of time, the trend of $d\theta/d[\ln(t^*)]$ over that time range was obtained by fitting the data with a linear function $\theta = -\alpha \ln(t^*) + \beta$. To calculate σ^* for each experiment, we use the initial angle value, θ_i from the time period the data fit is done over [see Fig. 1(e)]. t^* is the dimensionless time $t^* = t/\tau/(P_{\mathrm{drag}}/P_0)$. We use the characteristic timescale $\tau = L^2\eta/(\Delta\rho g d^3)$, used for drum experiments [11] (see details in Appendices B and C). For all our experiments τ is equal to 143 s. For pure avalanche experiments ($P_{\mathrm{drag}} = 0$), we use $1/\mathrm{Pe} \sim 10^{-9}$ instead of P_{drag}/P_0 to determine t^* and α accordingly.

Figure 3(a) presents the values of α as a function of P_{drag}/P_0, with colors representing series performed at different setup angles. First and importantly, due to the porous flow, measurable deformations are found until far under the yield criterion ($\theta_i \ll \theta_{\mathrm{stop}}$); relaxation is even observed for angles lower than 6°, the angle of repose for frictionless particles. The dashed gray curve represents the observation of α as a function of $1/\mathrm{Pe}$ for Brownian heaps [11]. Interestingly, part of our experiments have an order of magnitude of α comparable to the Brownian case, but mostly present different trends, and are quite scattered.

Figure 3(b) presents the value of α as a function of σ^*/σ_c^*, using $\sigma^* = \tan\theta_i/[1 - P_{\mathrm{drag}}/(P_0 3\cos\theta_i\cos\theta_{\mathrm{ap}})]$. Data illustrate how the distance to the critical stress is another important factor impacting the creep dynamics. We consider now the simple argument that, at a given intensity, the porous flow eventually triggers particle rearrangements of a characteristic length (or correlation length) $\xi \geqslant d$, and that it is a function of the shear stress in the vicinity of the critical stress. Recent simulation studies of subyield deformation of dry particulate material showed that $\xi/d \propto |\sigma_c^* - \sigma^*|^{-\nu}$, with ν found equal to 1/2 up to 1.8 depending on the measurement criteria [18,26].

Guided by this argument, we present our results as a function of a new parameter combining multiplicatively the observed effects of porous flow intensity and the distance to the critical stress on the creep rate:

$$P^* = \frac{P_{\mathrm{drag}}}{P_0}(\sigma_c^* - \sigma^*)^{-\nu} \propto \frac{P_{\mathrm{drag}}}{P_0}\xi/d. \tag{1}$$

In Fig. 3(c) the data of logarithmic decay α are reported as a function of P^* using $\nu = 3/4$, which successfully provides a collapse of all the data of deformation logarithmic rates. The collapse remains satisfying in the range $2/3 \leqslant \nu \leqslant 1$ (see Supplemental Material Fig. 3), which is consistent with the previous studies cited above.

We propose that the data collapse with P^* has the following physical basis. The system creep rate results from the product of two factors: the mean flow shear stress in the pores and the characteristic

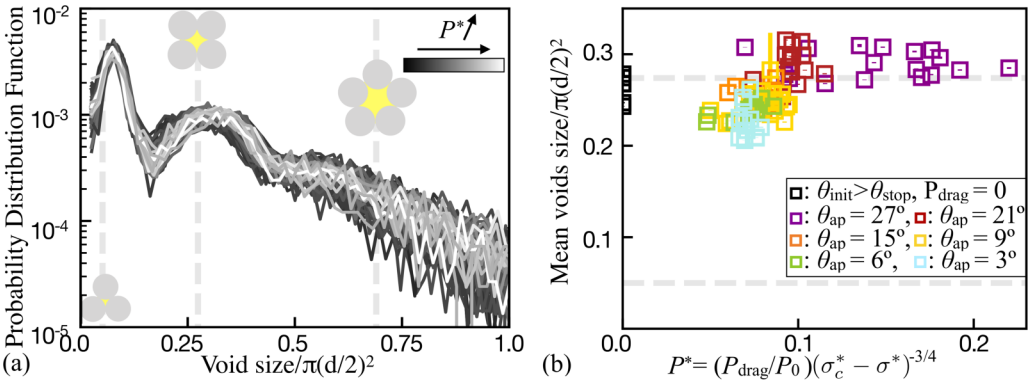

FIG. 4. (a) Probability distribution functions of the population of detected void sizes, for the last image at each experimental condition. The gray scale of the curves is proportional to the respective P^* value. (b) Mean void size, averaged over space and time, reported as a function of P^*. Gray dashed lines represent the geometric values for the void area between three cylinders, and four cylinders.

size of the areas susceptible to deform in the connected system. P^* can then be interpreted as an effective fluid flow force applied, via the pore network, on the system "soft spots," which are persistently reorganizing spatially but are of a given size for a given shear stress.

The inset of Fig. 3(c) shows the values of $(\sigma_c^* - \sigma^*)^{-3/4}$ in our experiments, represented as a function of σ^*/σ_c^*. Remarkably, it ranges from about 1 to about 10 for our experiments closest to the critical stress, which would be sensible values of rearrangement length scales in our experiments. Moreover, two very distinct trends are followed by the logarithmic decay rate presented as a function of P^*. These are seen in Fig. 3, for $0 < P^* \lesssim 0.1$ and $P^* \gtrsim 0.1$. To aid in seeing these trends, we present in the figure two functions which visually capture the two regimes: $\alpha = 130\exp(P^* - 0.095)$ for $P^* \lesssim 0.1$ and $\alpha = 13P^*$ for $P^* \gtrsim 0.1$.

The linear dependence of the decay rate α with P^* for $P^* \geqslant 0.1$ interestingly echoes the results of downslope creep triggered by weak Brownian agitation [11]. Yet, the necessity of using P^* to reconcile our data does not support that a model of hoping particles at the bed surface has straightforward application to the case of creep triggered by porous flow. Also, the abrupt fall of α as P^* decreases under 0.1, is a sharp difference, and a reminder that, unlike temperature, upward porous flow has a very nonlinear effect on a granular layer [10].

To enlighten the change of trend at $P^* \simeq 0.1$, we present in Fig. 4(a) measurements of VSD (void size distribution) from the final image of all the experiments, which are representative of the distribution at any time, although some slight time evolution can be observed. Void sizes are normalized by the projected area S_p, which allows for comparison with three theoretical values for the void space in a perfectly 2D layer of settled particles: the area between (1) three cylinders $(\sqrt{3}/\pi - 1/2)S_p \simeq 0.05S_p$, (2) four cylinders $(4/\pi - 1)S_p \simeq 0.27S_p$, and (3) five cylinders $\simeq 0.68S_p$. These values are marked by vertical dashed lines. All distributions present two main peaks which correspond to voids made by three and four contacting particles.

On first approximation all VSD curves fall on top of each other; yet, a minute shift to the right of the second peak occurs as P^* increases. This is consistent with Fig. 4(b), showing the average void size (computed over the fitting time windows used to determine α) as a function of P^*. Interestingly, the transition at $P^* \simeq 0.1$ observed in Fig. 3(a) is also marked in terms of microscopic structure, as it corresponds to where the mean void size crosses the characteristic value of the voids made by four cylinders in contact: $S_v/S_p \simeq 0.27$. This observation could be connected to the transition from a frictional-sliding dominated flow regime to a rolling-dominated one [27].

More observations will be necessary to confirm our physical interpretations of P^*; in particular, varying the system size, particle surface properties, and particle-fluid interaction properties would likely provide valuable new information.

We reported here novel experimental observations of subyield granular deformation under gravity and weak porous flow stresses. The tilted layer of grains exhibits a varying logarithmic decay of its slope with time. We reconcile all our observations by proposing a new parameter, P^*, combining the dimensionless flow pressure and distance to the critical stress. Future work documenting on both contacts and porous flow stress networks in frictional particulate systems, will be needed to develop intermediate-scale modeling of the reported dynamics. Such approach would open new perspectives on modeling the long-time dynamics and failure of wet granular systems, and soils and sea beds in particular.

This research was supported by the Levich Fellowship to M.H.; partially by National Science Foundation Grant No. 1605283 to J.F.M.; and by National Science Foundation Grant No. CBET 1512358 to C.M. M.H. thanks M. D. Shattuck, M. Wyart, and A. Bérut for fruitful discussions on the dynamics in the specific system, R. C. Sidle and G. E. Tucker for inspiring discussions on soil creep and avalanching modeling, and D. Mohrig for pointing out that the experiment was directly relevant to sea beds dynamics. Finally, M.H. thanks referee C for their constructive criticism which particularly helped to strengthen the manuscript.

APPENDIX A: DETERMINATION OF THE CRITICAL ANGLE θ_{stop}

Specific experiments were performed to assess the value of θ_{stop}, where the sediment layer is not initialized with its surface parallel to the grid, but as piled in the right corner, tilting the apparatus to an angle $\theta_{\text{ap}} = -18^\circ$. This allows for avalanching to happen longer and stop before the sediment layer becomes parallel to the grid. At the same time the camera starts capturing images, the apparatus is tilted to $\theta_{\text{ap}} = +28^\circ$, and no flow is imposed as the sediment layer avalanches down. This protocol was repeated four times, and the bed surface evolution results are shown in Supplemental Material: Ref. [20]. We measured the avalanche stop angle at 10^5 s (the longest duration investigated with this apparatus) as $\theta_{\text{stop}} = 32 \pm 0.5^\circ$.

APPENDIX B: DETERMINATION OF THE TIMESCALE τ

As our bed surface deformations (changes of the surface angle $d\theta$) remain small, we use the timescale one can determine for suspension in a drum: a cylinder of radius $L/2$. For $1 \ll L/d \ll \infty$, a characteristic timescale of deformation comes from volume conservation in the system. For a volume element of height h at the center of the drum where particle flow occurs at a velocity v, conservation of volume in the drum relates the flow rate, hv, to the change of bed geometry in the drum: $hv = 2(L/2)^2 d\theta/dt$. Assuming that the characteristic scale for h is the particle size, d, and the characteristic scale for v is the settling velocity $\propto \Delta\rho g d^2/\eta$, the resulting characteristic timescale is $\tau \propto L^2\eta/(\Delta\rho g d^3)$.

APPENDIX C: FITTING PROTOCOL OF $\theta(t^*)$ DATA

The finiteness of the channel dimensions and of the total volume of fluid injected into the system—related to the syringe choice, avoiding jerkiness issues met at slow injection rates—constrain the maximum duration over which we can observe our system dynamics and the minimum value of α we can measure. With an infinite observation time, all our creep experiments would exhibit an s-shaped deformation as a function of time (as shown in Fig. 1) with a final saturation plateau at a given value of θ, which has no physical meaning other than the deformation has met the dimension limit of the channel. Large deformations in our system also eventually means that the condition of porous flow significantly changed.

For these reasons and in order to best quantify the creep dynamics, we fit the data following the rules (1) to not consider the late trends of the slower slope of θ with $\log(t^*)$; (2) to not consider the first 40 s of our measurement, as it partly reflects the preinitial condition of no motion (see Fig. 2); (3) to fit the largest slope, over a minimum of one order of 10 of t^*; and (4) to use in our analysis the value of the surface angle at the initial time of the fit (θ_i), to consider the stress from which the logarithmic decay measured took place.

[1] M. Vandamme and F.-J. Ulm, Nanogranular origin of concrete creep, Proc. Natl. Acad. Sci. USA **106**, 10552 (2009).

[2] P. Cao, M. P. Short, and S. Yip, Understanding the mechanisms of amorphous creep through molecular simulation, Proc. Natl. Acad. Sci. USA **114**, 13631 (2017).

[3] J. T. Perron, J. W. Kirchner, and W. E. Dietrich, Formation of evenly spaced ridges and valleys, Nature (London) **460**, 502 (2009).

[4] B. Ferdowsi, C. P. Ortiz, and D. J. Jerolmack, Glassy dynamics of landscape evolution, Proc. Natl. Acad. Sci. USA **115**, 4827 (2018).

[5] D. J. Jerolmack and K. E. Daniels, Viewing Earth's surface as a soft-matter landscape, Nat. Rev. Phys. **1**, 716 (2019).

[6] O. Pouliquen, Scaling laws in granular flows down rough inclined planes, Phys. Fluids **11**, 542 (1999).

[7] S. Deboeuf, E. M. Bertin, E. Lajeunesse, and O. Dauchot, Jamming transition of a granular pile below the angle of repose, Eur. Phys. J. B **36**, 105 (2003).

[8] A. Pons, A. Amon, T. Darnige, J. Crassous, and E. Clément, Mechanical fluctuations suppress the threshold of soft-glassy solids: The secular drift scenario, Phys. Rev. E **92**, 020201(R) (2015).

[9] N. Gaudel, S. K. de Richter, N. Louvet, M. Jenny, and S. Skali-Lami, Granular avalanches down inclined and vibrated planes, Phys. Rev. E **94**, 032904 (2016).

[10] M. Houssais, C. Maldarelli, and J. F. Morris, Soil granular dynamics on-a-chip: Fluidization inception under scrutiny, Lab Chip **19**, 1226 (2019).

[11] A. Bérut, O. Pouliquen, and Y. Forterre, Brownian Granular Flows Down Heaps, Phys. Rev. Lett. **123**, 248005 (2019).

[12] K. Nichol, A. Zanin, R. Bastien, E. Wandersman, and M. van Hecke, Flow-Induced Agitations Create a Granular Fluid, Phys. Rev. Lett. **104**, 078302 (2010).

[13] K. A. Reddy, Y. Forterre, and O. Pouliquen, Evidence of Mechanically Activated Processes in Slow Granular Flows, Phys. Rev. Lett. **106**, 108301 (2011).

[14] O. Pouliquen, Y. Forterre, and S. Le Dizes, Slow dense granular flows as a self-induced process, Adv. Complex Syst. **4**, 441 (2001).

[15] K. Kamrin and M. Z. Bazant, Stochastic flow rule for granular materials, Phys. Rev. E **75**, 041301 (2007).

[16] J. Goyon, A. Colin, G. Ovarlez, A. Ajdari, and L. Bocquet, Spatial cooperativity in soft glassy flows, Nature (London) **454**, 84 (2008).

[17] K. Kamrin and G. Koval, Nonlocal Constitutive Relation for Steady Granular Flow, Phys. Rev. Lett. **108**, 178301 (2012).

[18] M. Bouzid, M. Trulsson, P. Claudin, E. Clément, and B. Andreotti, Nonlocal Rheology of Granular Flows Across Yield Conditions, Phys. Rev. Lett. **111**, 238301 (2013).

[19] G. Gauthier and P. Gondret, Compaction of liquid immersed granular packings by small upward flows, Phys. Rev. Fluids **4**, 074308 (2019).

[20] See Supplemental Material at http://link.aps.org/supplemental/10.1103/PhysRevFluids.6.L012301 for complementary information and data figures.

[21] M. Houssais, C. P. Ortiz, D. J. Durian, and D. J. Jerolmack, Rheology of sediment transported by a laminar flow, Phys. Rev. E **94**, 062609 (2016).

[22] D. Allan, C. van der Wel, N. Keim, T. A. Caswell, D. Wieker, R. Verweij, C. Reid, Thierry, L. Grueter, K. Ramos, apiszcz, zoeith, R. W. Perry, F. Boulogne, P. Sinha, pfigliozzi, N. Bruot, L. Uieda, J. Katins, H. Mary, and A. Ahmadia, soft-matter/trackpy: Trackpy v0.4.2, Zenodo (2019), doi: 10.5281/zenodo.3492186.

[23] J. J. Roering, J. W. Kirchner, and W. E Dietrich, Evidence for nonlinear, diffusive sediment transport on hillslopes and implications for landscape morphology, Water Resour. Res. **35**, 853 (1999).

[24] S. S. Vyalov, *Rheological Fundamentals of Soil Mechanics* (Elsevier, New York, 1986).

[25] V. B. Nguyen, T. Darnige, A. Bruand, and É. Clément, Creep and Fluidity of a Real Granular Packing Near Jamming, Phys. Rev. Lett. **107**, 138303 (2011).

[26] J. D. Thompson and A. H. Clark, Critical scaling for yield is independent of distance to isostaticity, Phy. Rev. Res. **1**, 012002 (2019).

[27] M. Trulsson, E. DeGiuli, and M. Wyart, Effect of friction on dense suspension flows of hard particles, Phys. Rev. E **95**, 012605 (2017).